

The ionization fraction gradient across the Horsehead edge: An archetype for molecular clouds[★]

J.R. Goicoechea¹, J. Pety^{2,3}, M. Gerin³, P. Hily-Blant⁴, and J. Le Bourlot⁵

¹ Laboratorio de Astrofísica Molecular. Centro de Astrobiología. CSIC-INTA.

Carretera de Ajalvir, Km 4. Torrejón de Ardoz, 28850, Madrid, Spain. e-mail: goicoechea@damir.iem.csic.es

² IRAM, 300 rue de la Piscine, 38406 Grenoble cedex, France.

e-mail: pety@iram.fr

³ LERMA-LRA, UMR 8112, CNRS, Observatoire de Paris and Ecole Normale Supérieure, 24 Rue Lhomond, 75231 Paris, France.

e-mail: maryvonne.gerin@lra.ens.fr

⁴ Laboratoire d'Astrophysique, Observatoire de Grenoble, BP 53, 38041 Grenoble Cedex 09, France.

e-mail: pierre.hilyblant@obs.ujf-grenoble.fr

⁵ LUTH, UMR 8102 CNRS, Université Paris 7 and Observatoire de Paris, Place J. Janssen 92195 Meudon, France.

e-mail: Jacques.Lebourlot@obspm.fr

Received 10 December 2008 / Accepted 11 February 2009

ABSTRACT

Context. The ionization fraction (*i.e.*, the electron abundance) plays a key role in the chemistry and dynamics of molecular clouds.

Aims. We study the H¹³CO⁺, DCO⁺ and HOC⁺ line emission towards the Horsehead, from the shielded core to the UV irradiated cloud edge, *i.e.*, the Photodissociation Region (PDR), as a template to investigate the ionization fraction gradient in molecular clouds.

Methods. We analyze an IRAM Plateau de Bure Interferometer map of the H¹³CO⁺ $J=1-0$ line at a 6.8'' × 4.7'' resolution, complemented with IRAM-30m H¹³CO⁺ and DCO⁺ higher- J line maps and new HOC⁺ and CO⁺ observations. We compare self-consistently the observed spatial distribution and line intensities with detailed depth-dependent predictions of a PDR model coupled with a non-local radiative transfer calculation. The chemical network includes deuterated species, ¹³C fractionation reactions and HCO⁺/HOC⁺ isomerization reactions. The role of neutral and charged PAHs in the cloud chemistry and ionization balance is investigated.

Results. The detection of HOC⁺ reactive ion towards the Horsehead PDR proves the high ionization fraction of the outer UV irradiated regions, where we derive a low [HCO⁺]/[HOC⁺] ≈ 75–200 abundance ratio. In the absence of PAHs, we reproduce the observations with gas-phase metal abundances, [Fe+Mg+...], lower than 4 × 10⁻⁹ (with respect to H) and a cosmic-rays ionization rate of ζ = (5 ± 3) × 10⁻¹⁷ s⁻¹. The inclusion of PAHs modifies the ionization fraction gradient and increases the required metal abundance.

Conclusions. The ionization fraction in the Horsehead edge follows a steep gradient, with a scale length of ~0.05 pc (or ~25''), from [e⁻] ≈ 10⁻⁴ (or n_e ~ 1.5 cm⁻³) in the PDR to a few times ~10⁻⁹ in the core. PAH⁻ anions play a role in the charge balance of the cold and neutral gas if substantial amounts of free PAHs are present ([PAH] > 10⁻⁸).

Key words. Astrochemistry – ISM clouds – molecules – individual object (Horsehead nebula) – radiative transfer – radio lines: ISM

1. Introduction

The electron abundance ([e⁻] = n_e/n_H) plays a fundamental role in the chemistry and dynamics of interstellar gas. The degree of ionization determines the preponderance of ion-neutral reactions, *i.e.*, the main formation route for most chemical species in molecular clouds (Herbst & Klemperer 1973, Oppenheimer & Dalgarno 1974). In addition, the ionization fraction constrains the coupling of matter and magnetic fields, which drives the dissipation of turbulence and the transfer of angular momentum, thus having crucial implications in protostellar collapse and accretion disks (*e.g.*, Balbus & Hawley 1991).

High-angular resolution observations of interstellar clouds reveal steep density, temperature and turbulence gradients as well as sharp chemical variations. Accordingly, the electron abundance should vary within a cloud depending on the relative ionizing sources and prevailing chemistry.

Send offprint requests to: e-mail: goicoechea@damir.iem.csic.es

[★] Based on observations obtained with the IRAM Plateau de Bure interferometer and 30 m telescope. IRAM is supported by INSU/CNRS (France), MPG (Germany), and IGN (Spain).

Rotational line emission of molecular ions such as DCO⁺ and HCO⁺ have been traditionally used to estimate the ionization fraction in molecular clouds because (*i*) they are abundant and easily observable (*ii*) dissociative recombination is their main destruction route, and thus their abundances are roughly inversely proportional to the electron abundance (*e.g.*, Guélin et al. 1982, Wootten et al. 1982, de Boisanger et al. 1996, Williams et al. 1998, Caselli et al. 1998, Maret & Bergin 2007, Hezareh et al. 2008). On the other hand, the presence of reactive ions (species such as HOC⁺ or CO⁺ that react rapidly with H₂) is predicted to be a sensitive indicator of high ionization fraction regions, *e.g.*, the UV irradiated cloud surfaces (*e.g.*, Smith et al. 2002, Fuente et al. 2003).

In order to constrain the ionization fraction gradient from models, the cloud chemistry and physics can not be simplified much because the charge balance depends on parameters such as the penetration of UV radiation, the cosmic-rays ionization rate (ζ) and the abundance of key species (*e.g.*, metals and PAH).

Compared to other works, in this paper we determine the ionization fraction gradient by direct comparison of H¹³CO⁺ and DCO⁺ high-angular resolution maps and HOC⁺ pointed ob-

Table 1. Observation parameters of the PdBI maps shown in Figure 1.

Molecule	Transition	Frequency GHz	Instrument	Config.	Beam arcsec	PA °	Vel. Resol. km s ⁻¹	Int. Time ^a hours	T _{sys} K	Noise ^{b,†} K	Obs. date
H ¹³ CO ⁺	1-0	86.754288	PdBI	C & D	6.8 × 4.7	13	0.2	6.5	150	0.10	2006-07
HCO	1 _{0,1} 3/2, 2-0 _{0,0} 1/2, 1	86.670760	PdBI	C & D	6.7 × 4.4	16	0.2	6.5	150	0.09	2006-07

^a We observed a 7-field mosaic centered on the IR peak at $\alpha_{2000} = 05^h40^m54.27^s$, $\delta_{2000} = -02^\circ28'00''$ (Abergel et al. 2003) with the following offsets: $(-5.5'', -22.0'')$, $(5.5'', -22.0'')$, $(11.0'', 0.0'')$, $(0.0'', 0.0'')$, $(-11.0'', 0.0'')$, $(-5.5'', 22.0'')$ and $(5.5'', 22.0'')$. The total field-of-view is $80.1'' \times 102.1''$ and the half power primary beam is $58.1''$. The mosaic was Nyquist sampled in declination at 3.4 mm and largely oversampled in right ascension. This maximizes the field of view along the PDR edge while the oversampling in the perpendicular direction eases the deconvolution. On-source time computed as if the source were always observed with 6 antennae. ^b The noise values refer to the mosaic phase center (mosaic noise is inhomogeneous due to primary beam correction; it steeply increases at the mosaic edges).

Table 2. Observation parameters of the IRAM-30m observations.

Molecule	Transition	Frequency GHz	Instrument	F_{eff}	B_{eff}	Resol. arcsec	Resol. km s ⁻¹	Int. Time hours	Noise [†] K	Observing Mode	Obs. date
HCO ⁺	$J=1-0$	89.188523	30m/A100	0.95	0.78	27.6''	0.20	4.7	0.02	ON-OFF	2008
HOC ⁺	$J=1-0$	89.487414	30m/A100	0.95	0.78	27.5''	0.20	4.7	0.02	ON-OFF	2008
CO ⁺	2, 5/2-1, 3/2	236.062578	30m/A230	0.91	0.52	10.4''	0.20	4.7	0.05	ON-OFF	2008
H ¹³ CO ⁺	$J=1-0$	86.754288	30m/AB100	0.95	0.78	28.4''	0.20	2.6	0.10	OTF map	2006-07
H ¹³ CO ⁺	$J=3-2$	260.255339	30m/HERA	0.90	0.46	13.5''	0.20	5.9	0.06	OTF map	2006
DCO ⁺	$J=2-1$	144.077289	30m/CD150	0.93	0.69	18.0''	0.08	5.9	0.18	OTF map	2006
DCO ⁺	$J=3-2$	216.112582	30m/HERA	0.90	0.52	11.4''	0.11	1.5	0.10	OTF map	2006

[†] The noise (in T_{mb} scale) refers to the channel spacing obtained by averaging adjacent channels to the velocity resolution given in the tables.

servations, with detailed depth-dependent chemical and radiative transfer models covering a broad range of cloud physical conditions. Indeed, the observed field-of-view contains the famous Horsehead PDR (the UV illuminated edge of the cloud) and a dense and cold core discovered by us from its intense DCO⁺ line emission (Pety et al. 2007). Due to its simple geometry and moderate distance ($d \simeq 400$ pc), the Horsehead PDR and associated core are good templates to study the steep gradients expected in molecular clouds (*e.g.*, Pety et al. 2005, 2007, Goicoechea et al. 2006, Gerin et al. 2009).

The paper is organized as follows. The observations are presented in Sect. 2 and the models used to interpret them are described in Sect. 3. The chemistry of H¹³CO⁺, DCO⁺ and HOC⁺ (our observational probes of the ionization fraction) is analyzed in Sect. 4. In Sect. 5 we investigate the role of metals, PAHs and ζ on the electron abundance determination. The main results and constraints are presented in Sect. 6 and discussed in Sect. 7.

2. Observations

2.1. Observations and data reduction

Tables 1 and 2 summarize the observation parameters of the data obtained with the PdBI and the IRAM-30m telescope that we shall study in this work. The H¹³CO⁺ $J=1-0$ line emission map was first presented in Gerin et al. (2009). Frequency-switched, on-the-fly maps (OTF) obtained at the IRAM-30m were used to produce the short-spacings needed to complement a 7-field mosaic acquired with the 6 PdBI antennae in the CD configuration (baseline lengths from 24 to 176 m). Correlator backends were used (VESPA for IRAM-30m observations). The high angular resolution PdBI H¹³CO⁺ $J=1-0$ map complements our previous H¹³CO⁺ $J=3-2$ and DCO⁺ $J=2-1$ and $3-2$ maps taken with the IRAM-30m telescope and first presented in Pety et al. (2007).

In this work we present new IRAM-30m deeper integrations in the HOC⁺, H¹³CO⁺ and HCO⁺ $J=1-0$ lines, and an upper limit for the CO⁺ emission towards the PDR (defined here as the HCO emission peak; Gerin et al. 2009). The position switching observing mode was used. The on-off cycle duration was 1 minute

and the off-position offsets were $(\Delta\alpha, \Delta\delta) = (-100'', 0'')$, *i.e.*, the H II region ionized by σ Ori and free of molecular gas emission. Position accuracy is estimated to be $\sim 3''$ for the 30m data and better than $0.5''$ for the PdBI data. The data processing was done with the GILDAS¹ softwares (*e.g.*, Pety 2005b). The IRAM-30m data were first calibrated to the T_A^{*} scale using the chopper wheel method (Penzias & Burrus 1973), and finally converted to main beam temperatures T_{mb} using the forward and main beam efficiencies F_{eff} and B_{eff} displayed in Table 2 (*e.g.*, Greve et al. 1998). The amplitude accuracy for heterodyne observations with the IRAM-30m telescope is $\sim 10\%$. PdBI data and short-spacing data were merged before imaging and deconvolution of the mosaic, using standard techniques of GILDAS and used in our previous works (see *e.g.*, Pety et al. 2005).

2.2. DCO⁺ and H¹³CO⁺ spatial distribution, HOC⁺ detection

Figure 1 shows H¹³CO⁺ $J=1-0$, HCO 1_{0,1}-0_{0,0} (PdBI) and DCO⁺ $J=2-1$, $3-2$ integrated line intensity maps (IRAM-30m; Pety et al. 2007), as well as the Aromatic Infrared Band emission (AIB, observed with ISOCAM, Abergel et al. 2003) that traces the UV illuminated edge of the cloud, *i.e.*, the PDR. The DCO⁺ emission is concentrated in a narrow, arclike structure of dense and cold gas behind the PDR (Pety et al. 2007). Hence, it shows a very different spatial distribution than the emission of “PDR tracers” such as C₂H, C₄H, *c*-C₃H₂ (Pety et al. 2005), HCO radicals (Gerin et al. 2009), vibrationally excited H₂ (Habart et al. 2005) or the AIB emission (Compiègne et al. 2008). The H¹³CO⁺ $J=1-0$ emission follows the DCO⁺ distribution and it mostly delineates the dense core that coincides with the DCO⁺ emission peak. Nevertheless, while DCO⁺ is not detected in the illuminated edge, H¹³CO⁺ does show a faint emission in the PDR. Therefore, the small field-of-view shown in Fig. 1 contains two different environments: a warm PDR and a cold core shielded from the external UV radiation field. In the following sections we analyze these

¹ See <http://www.iram.fr/IRAMFR/GILDAS>

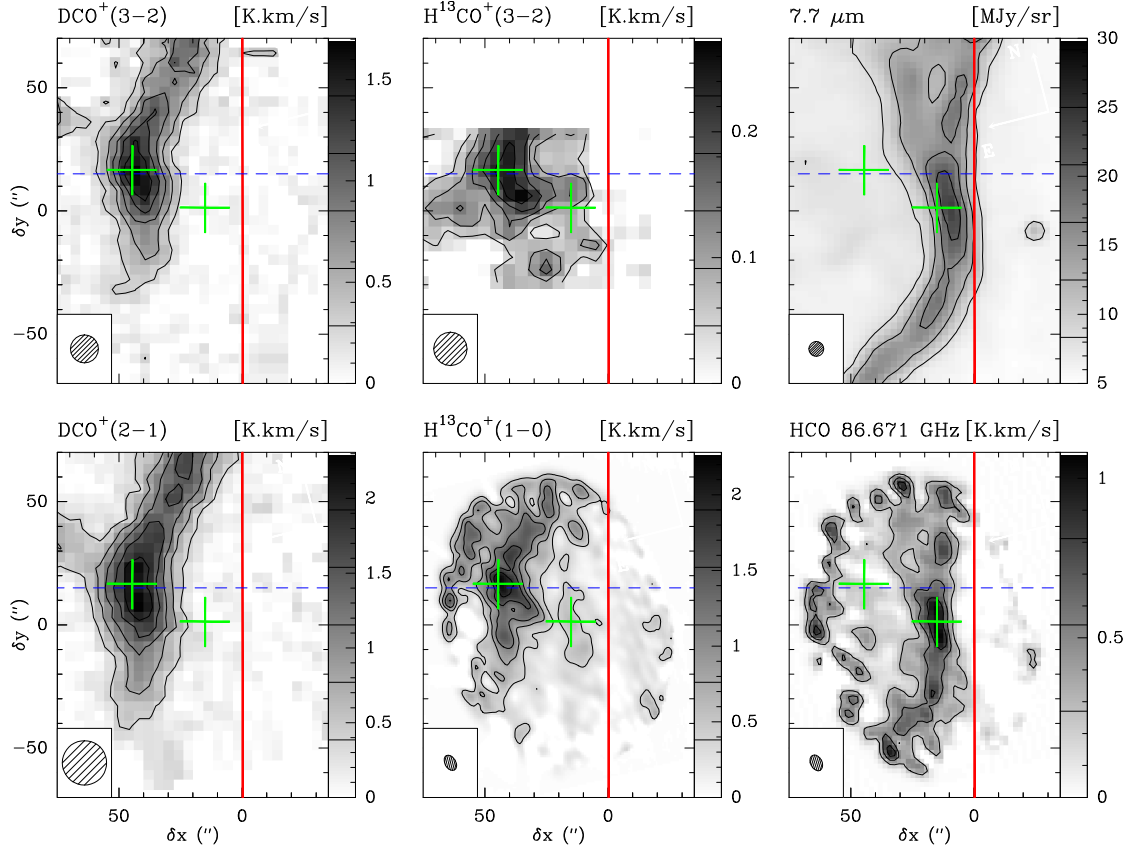


Fig. 1. DCO^+ $J=3-2$ and $2-1$ (IRAM-30m; from Pety et al. 2007), H^{13}CO^+ $J=1-0$ (PdBI) and $3-2$ (IRAM-30m) line integrated intensity maps, Aromatic Infrared Band emission (ISOCAM, from Abergel et al. 2003) and HCO^+ (PdBI, from Gerin et al. 2009). Maps have been rotated by 14° counter-clockwise around the projection center, located at $(\delta x, \delta y) = (20'', 0'')$ to bring the illuminated star direction in the horizontal direction. The horizontal zero has been set at the cloud edge ($\delta x=0''$). The H^{13}CO^+ , DCO^+ and HCO^+ emission is integrated between 10.1 and 11.1 km s^{-1} . Integrated intensities are expressed in the T_{mb} scale. Contour levels are displayed on the grey scale lookup tables. The red vertical line shows the PDR edge and the green crosses shows two representative positions: the “shielded core” (the DCO^+ emission peak at $\delta x \sim 45''$; Pety et al. 2007) and the “PDR” (the HCO^+ emission peak at $\delta x \sim 15''$; Gerin et al. 2009). The dashed blue line shows the horizontal cut analyzed in this work.

emission maps to determine the ionization fraction gradient in the region.

Figure 2 shows long integration spectra of the HOC^+ , H^{13}CO^+ and HCO^+ $J=1-0$ lines towards the PDR. This is the first detection of HOC^+ reactive ion towards the Horsehead, and adds to previous detections in interstellar environments with high electron abundances (Woods et al. 1983, Ziurys & Apponi 1995, Fuente et al. 2003, Rizzo et al. 2003, Savage & Ziurys 2004, Liszt et al. 2004). H^{12}CO^+ lines are optically thick, as shown by the low $\text{H}^{12}\text{CO}^+/\text{H}^{13}\text{CO}^+$ $J=1-0$ line intensity ratio (~ 7), much lower than the expected $^{12}\text{C}/^{13}\text{C} \approx 60$ abundance ratio (Langer & Penzias 1990, Savage et al. 2002) and references therein). The large opacity of H^{12}CO^+ lines even towards the PDR justifies the use of H^{13}CO^+ lines as tracers of the HCO^+ abundance.

3. Analysis: Models

In this work we couple the depth-dependent abundances predicted by a PDR model (for the varying physical conditions prevailing in the Horsehead edge) with detailed excitation and radiative transfer calculations adapted to the cloud geometry. This technique allows us to analyze different chemical models by direct comparison with observed line intensities. This methodology was introduced to study our interferometric CS and C^{18}O

Table 3. Main spectroscopic parameters of the studied lines.

Species	Transition $J_{\text{upp}} - J_{\text{low}}$	Frequency (GHz)	A_{ij} (s^{-1})	E_{upp} (K)
HCO^+	1-0	89.188523	4.2×10^{-5}	4.3
HOC^+	1-0	89.487414	2.2×10^{-5}	4.3
H^{13}CO^+	1-0	86.754288	3.9×10^{-5}	4.2
CO^+	$2(5/2)-1(3/2)$	236.062578	4.7×10^{-4}	17.2
H^{13}CO^+	3-2	260.255339	1.3×10^{-3}	25.0
DCO^+	2-1	144.077289	2.1×10^{-4}	10.4
DCO^+	3-2	216.112582	7.7×10^{-4}	20.7

maps of the Horsehead edge (Goicoechea et al. 2006). It enables to observationally benchmark the abundance gradients predicted by chemical models, even if it does not produce perfect fits to line profiles in all cloud positions. In this paper, we analyze a horizontal cut of the H^{13}CO^+ and DCO^+ line emission along the direction of the illuminating star ($\delta y=15''$). Figure 1 shows that this cut (blue dashed line) goes across the DCO^+ emission peak ($\delta x \sim 45''$), which we identify as the “shielded core”, and across the HCO^+ emission peak, the “PDR” ($\delta x \sim 15''$).

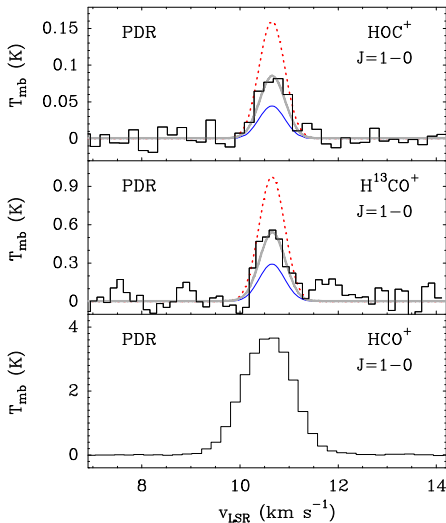


Fig. 2. HOC^+ and H^{13}CO^+ $J=1-0$ lines towards the Horsehead PDR (upper and middle panels) observed with the IRAM-30m telescope. Solid lines are radiative transfer models with $T_k=60$ K, $n(\text{H}_2)=5\times 10^4$ cm^{-3} , $n(\text{H})=500$ cm^{-3} and $[e^-]=5\times 10^{-5}$. Three different abundances are shown, grey thick line: $[\text{HOC}^+]=4.0\times 10^{-12}$ and $[\text{H}^{13}\text{CO}^+]=1.5\times 10^{-11}$; red dashed line: abundances $\times 2$; blue thin line: abundances $\div 2$. For completeness, the HCO^+ $J=1-0$ line towards the PDR is also shown (lower panel). This transition is very opaque, as shown by the low $\text{H}^{12}\text{CO}^+/\text{H}^{13}\text{CO}^+$ $J=1-0$ line intensity ratio (~ 7). The resulting line profile is thus broadened and it suffers from scattering by low-density foreground gas that we do not model here.

3.1. Geometry and density gradient

The Horsehead edge has an almost edge-on geometry with a line-of-sight depth of $l_{\text{depth}} \approx 0.1$ pc (e.g., Habart et al. 2005) and a spatial scale in the plane of the sky of ≈ 0.002 pc arcsec $^{-1}$. We determine the density profile from observations by fitting the 1.2 mm dust continuum emission (IRAM-30m/MAMBO) along the $\delta y=15''$ direction (Hily-Blant et al. 2005). In this fit, we adopt a dust opacity per unit (gas+dust) mass column density of $\kappa_{1.2}=0.003$ cm^2 g^{-1} at 1.2 mm (computed for “MRN grains”: Mathis, Rumpl & Nordsieck 1977, see below), our best knowledge of the dust grains temperature (from ~ 15 K in the core to ~ 30 K in the PDR; e.g., Ward-Thompson et al. 2006) and a power-law density profile $n_H(r)=n(\text{H})+2n(\text{H}_2) \propto r^{-p}$, where r is the distance from the shielded core towards the illuminated edge of the cloud. Best fits are obtained for a steep density gradient in the cloud edge ($p \approx 3$) and a flatter one towards the core ($p \approx 0.5$). The turnover point occurs at core radius of $r \approx 0.04$ pc (or $\delta x \approx 23''$ in the maps). The resulting density gradient used in the photochemical and radiative transfer models is shown in Fig. 4. In the next sections we constrain the ionization fraction gradient in the cloud by comparing synthetic and observed H^{13}CO^+ and DCO^+ spectra along the same cut.

3.2. Photochemical models

We have updated the *Meudon PDR code* to model our observations of the Horsehead. The code has been described in detail elsewhere (e.g., Le Bourlot et al. 1993, Le Petit et al. 2006, Goicoechea & Le Bourlot 2007) and benchmarked against other PDR codes by Röllig et al. (2007). In this section we summarize the most relevant upgrades and model features for this work.

3.2.1. UV radiative transfer and dust properties

The code solves the UV radiative transfer taking into account dust scattering and gas absorption. Anisotropic scattering of UV photons by dust grains is included by explicitly calculating the wavelength-dependent grain albedo and g -asymmetry parameters (Goicoechea & Le Bourlot 2007). This enables the specific computation of the UV radiation field (continuum+lines) and thus, the direct integration of consistent photoionization and photodissociation rates. We use two types of dust populations: (i) a mixture of graphite+silicate grains and (ii) PAHs (see next paragraph). More precisely, we adopt a power-law size distribution ($n(a) \propto a^{-3.5}$) with minimum and maximum radius of ~ 5 and ~ 250 nm respectively (for graphite+silicate grains). Wavelength-dependent optical properties (Q efficiencies and g factors) are interpolated from Laor & Draine (1993) tabulations. With a standard gas-to-dust mass ratio (~ 100), this grain mixture (“MRN grains”) reproduces the main characteristics of the standard interstellar extinction curve with $N_{\text{H}}/A_{\text{V}}=1.9\times 10^{21}$ cm^{-2} and $R_{\text{V}}=3.1$.

In order to complete our description of the dust populations, in this work we have also added smaller aromatic grains. Observationally, the AIB emission towards the Horsehead (produced by free PAHs according to the most accepted theory; Léger & Puget 1984, Allamandola et al. 1985) clearly separates the H II region and PDR (where the emission is bright) from the regions shielded from UV radiation, where no AIB emission is detected (Abergel et al. 2003, Habart et al. 2005, Compiègne et al. 2007, 2008). However, the size distribution and PAH abundance in dense regions shielded from UV radiation are uncertain. It may vary from “negligible”, if PAHs coagulate into larger PAH aggregates (Boulanger et al. 1990, Rapacioli et al. 2006) to “high” abundances (though they will not be detected in the mid-IR due to the lack of UV photons to excite them). We used the following PAH properties: a size distribution with ~ 0.4 and ~ 1.2 nm radii limits (Desert et al. 1990) and optical properties from Li & Draine (2001). This size distribution is compatible with PAHs having a mean radius of ~ 0.6 nm and $N_{\text{C}} \sim 100$ carbon atoms assuming $N_{\text{C}} \approx 500 a^3$ (Bakes & Tielens 1994). The extinction curve and the efficiency of the photoelectric heating mechanism depend on the mass fraction put into PAHs (Bakes & Tielens 1994). Depending on the PAH abundance, they contribute to the total dust mass by $\sim 1\%$ for $[\text{PAH}]=10^{-7}$ and $\sim 10\%$ for $[\text{PAH}]=10^{-6}$.

3.2.2. Chemical network and elemental abundances

Once the UV field is determined at every cloud position, steady-state chemical abundances are computed for a given network of chemical reactions. The model also computes the temperature profile by solving the thermal balance between the most important gas heating and cooling mechanisms (Le Petit et al. 2006). Our chemical network contains ~ 160 species and ~ 2000 reactions. It includes deuteration, ^{13}C fractionation (Graedel et al. 1982) and $\text{HCO}^+/\text{HOC}^+$ isomerization reactions. When available, we used the photodissociation rates given by van Dishoeck (1988), which are explicitly calculated for the Draine’s interstellar radiation field (ISRF). The most critical reaction rates for our determination of the ionization fraction are listed in Table 4. Most reactions were checked against *OSU* (E. Herbst and co-workers) and *UDFA* (Woodall et al. 2006) networks. Besides, we benchmarked our network with more extended ones by comparing the predicted abundances of simple species such as CO and DCO^+ .

Following Flower & Pineau des Forêts (2003), we have also included interactions (~ 60 reactions) of gas phase species with very small aromatic grains (neutral PAH and singly charged PAH $^\pm$). In particular, we take into account PAH-gas processes such as neutralization reactions of atomic and molecular cations on PAH $^-$, PAH electron attachment and photodetachment of PAH $^-$ and PAH by UV photons. Such processes can play a significant role in the ionization balance of dense molecular clouds (e.g., Lepp & Dalgarno 1988, Bakes & Tielens 1998, Flower et al. 2007, Wakelam & Herbst 2008, Wolfire et al. 2008). We have not included larger grains in the network in order to isolate the role of PAHs in the gas-phase chemistry. We thus assume that recombinations of ions with grains are much less frequent than recombinations with electrons and PAH $^-$. This is partially justified by the fact that, according to their size and mass, the fractional abundance of “MRN grains” is low: $n_g/n_H \approx 10^{-10}$ and their *effective* cross section per H nucleus is $(n_g/n_H)\pi a^2 \approx 10^{-21} \text{ cm}^{-2}$ (the product of the grains abundance and the mean grain cross section). Grain growth towards the denser parts of the cloud will result in even lower grain abundances and smaller *effective* cross sections if the gas-to-dust mass ratio has to be preserved: e.g., $(n_g/n_H) \approx 10^{-13}$ and $(n_g/n_H)\pi a^2 \approx 10^{-22} \text{ cm}^{-2}$ if the grain radii a increase by ~ 10 . Therefore, the resulting lower abundance of charged grains and their smaller *effective* cross section for ion-grain recombinations will not alter our estimations of the ionization fraction much.

Table 4. Key chemical reaction rates † adopted in this work.

Reaction	Rate [$\text{cm}^3 \text{ s}^{-1}$]
$\text{HCO}^+ + e^- \rightarrow \text{CO} + \text{H}$	$2.4 \times 10^{-7} (300 \text{ K}/T)^{0.69 a}$
$\text{HCO}^+ + \text{PAH}^- \rightarrow \text{PAH} + \text{CO} + \text{H}$	$1.4 \times 10^{-8} (300 \text{ K}/T)^{0.50 b}$
$\text{M}^+ + e^- \rightarrow \text{M} + h\nu$	$3.7 \times 10^{-12} (300 \text{ K}/T)^{0.65}$
$\text{M}^+ + \text{PAH}^- \rightarrow \text{M} + \text{PAH}$	$1.0 \times 10^{-8} (300 \text{ K}/T)^{0.50 b}$
$\text{C}^+ + \text{H}_2\text{O} \rightarrow \text{HCO}^+ + \text{H}$	$8.9 \times 10^{-10} (300 \text{ K}/T)^{0.50}$
$\text{C}^+ + \text{H}_2\text{O} \rightarrow \text{HOC}^+ + \text{H}$	$1.8 \times 10^{-9} (300 \text{ K}/T)^{0.50}$
$\text{CO}^+ + \text{H}_2 \rightarrow \text{HCO}^+ + \text{H}$	7.5×10^{-10}
$\text{CO}^+ + \text{H}_2 \rightarrow \text{HOC}^+ + \text{H}$	7.5×10^{-10}
$\text{HOC}^+ + \text{H}_2 \rightarrow \text{HCO}^+ + \text{H}_2$	$3.8 \times 10^{-10 c}$

† Rates are from the *UDFA (UMIST Database for Astrochemistry)* and *OSU (Ohio State University)* data bases unless indicated.

^a Cited in the text as $\alpha(\text{HCO}^+)$, it also applies to DCO^+ and H^{13}CO^+ .

^b Rate is from Flower & Pineau des Forêts 2003.

^c Rate is from Smith et al. 2002.

The adopted elemental abundances are shown in Table 5. Low ionization potential heavy *metals* ($\lesssim 8 \text{ eV}$; Fe^+ , Mg^+ or Na^+) are all represented by a single element, “M $^+$ ”. In our model, such metals slowly recombine with electrons (through radiative recombinations), can be photoionized and can exchange charge with ions and neutrals (including PAHs). However, they are assumed to be chemically inert and thus do not form *metallic* molecules (e.g., Oppenheimer & Dalgarno 1974).

Once the physical and geometrical parameters of the cloud are constrained, the only free parameters in the model are the cosmic-rays ionization rate and the metal and PAH abundances.

3.3. From abundances to spectra: mm radiative transfer

We use the PDR model predictions (molecular abundance, $n(\text{H}_2)$, $n(\text{H})$, gas temperature and ionization fraction gradients) as input for a nonlocal radiative transfer calculation able to com-

Table 5. Standard conditions and gas-phase elemental abundances. Abundances, noted [x], refer to H.

Parameter	Value
Radiation field χ	60 (Draine units)
Density $n_H(r)=n(\text{H}) + 2n(\text{H}_2)$	$\propto r^{-3}$, up to $\sim 2 \times 10^5 \text{ cm}^{-3}$
Line of sight depth l_{depth}	0.1 pc
$[\text{He}]=n(\text{He})/n_H$	1.00×10^{-1}
[O]	3.02×10^{-4}
[^{12}C]	1.38×10^{-4}
[N]	7.95×10^{-5}
[D]	1.60×10^{-5}
[S]	3.50×10^{-6}
$[^{13}\text{C}]=[^{12}\text{C}]/60$	2.30×10^{-6}
[PAH]	variable: $0\text{--}10^{-7}$
[metals] \equiv [M] \equiv [Fe + Mg + ...]	variable: $10^{-11}\text{--}10^{-5}$
Cosmic ray ionization rate ζ	variable: $10^{-18}\text{--}10^{-15} \text{ s}^{-1}$

pute DCO^+ and H^{13}CO^+ line intensities as a function of cloud position. Our radiative transfer code handles edge-on plane-parallel geometry, and accounts for line trapping, collisional excitation 2 , and radiative excitation by absorption of continuum photons. After the level populations are determined in each modeled slab, emergent line intensities along each line of sight are computed and convolved with the telescope angular resolution at each frequency. A more detailed description is given in Goicoechea et al. (2006; Appendix). Since typical densities in the Horsehead ($\sim 10^4\text{--}10^5 \text{ cm}^{-3}$) are below the critical densities of the observed high-dipole moment molecular ions (a few $\sim 10^5\text{--}10^6 \text{ cm}^{-3}$ for the studied transitions) our approach allows us to properly take into account non-LTE excitation effects (e.g., sub-thermal excitation), as well as opacity and line profile formation.

4. Chemistry of the ionization fraction probes

4.1. H^{13}CO^+ and DCO^+ chemistry in the UV shielded core

The detection of very bright DCO^+ emission towards the shielded core (Pety et al. 2007) implies cold gas temperatures ($T_k \approx 10\text{--}20 \text{ K}$) and thus efficient HCO^+ deuterium fractionation (i.e., $[\text{DCO}^+]/[\text{HCO}^+] \gg \text{D}/\text{H}$). From our observations we infer $[\text{DCO}^+] \approx 8.0 \times 10^{-11}$, $[\text{H}^{13}\text{CO}^+] \approx 6.5 \times 10^{-11}$ and thus a $[\text{DCO}^+]/[\text{HCO}^+] \approx 0.02$ abundance ratio towards the core peak. Such gas-phase DCO^+ enhancement is achieved via reaction:



which is endothermic by $\sim 232 \text{ K}$ in the right-to-left direction (Gerlich et al. 2002), followed by

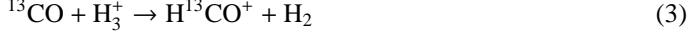


which dominates the DCO^+ formation in the cold and dense gas. The absence of significant DCO^+ line emission in the PDR is consistent with the higher temperatures ($>60 \text{ K}$) expected in the illuminated edge of the cloud.

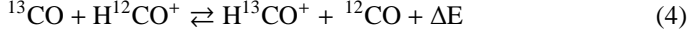
Besides, the detection of intense H^{13}CO^+ emission towards the shielded core and its vicinity (see Fig. 1) implies low

² PDR-like environments require to consider inelastic collisions with H_2 , H, He and e^- . H^{13}CO^+ , DCO^+ and HOC^+ collisional rates with H_2 , H and He have been scaled from those of Flower (1999), while collisional rates with e^- were kindly provided by A. Faure and J. Tennyson (see e.g., Faure & Tennyson 2001).

ionization fractions. In terms of excitation and opacity effects, H^{13}CO^+ is a much more reliable tracer of HCO^+ column density than H^{12}CO^+ itself (as the latter suffers from very large opacities and line photon scattering by low-density halos; *e.g.*, Cernicharo & Guélin 1987). In terms of its chemistry, two main processes dominate the formation of H^{13}CO^+ in the low temperature shielded gas:



and isotopic fractionation through



which is endothermic by only ~ 9 K in the right-to-left direction (Langer et al. 1984) and competes with dissociative recombination in the destruction of H^{13}CO^+ where the abundance of electrons is low. For the physical conditions prevailing in the shielded core, we predict $[\text{H}^{12}\text{CO}^+]/[\text{H}^{13}\text{CO}^+]$ abundance ratios down to ~ 0.7 times lower than the elemental $[^{12}\text{C}]/[^{13}\text{C}]$ isotopic ratio. Since both H^{13}CO^+ and DCO^+ are mainly destroyed by fast dissociative recombination with electrons:



their abundances inversely scale with that of electrons. In this work we have used a “standard” HCO^+ dissociative recombination rate (*i.e.*, $\alpha(\text{HCO}^+) = 2.4 \times 10^{-7} (300/T)^{0.69} \text{ cm}^3 \text{ s}^{-1}$) recommended in most astrochemical data bases. We note, however, that there is a certain discrepancy among different theoretical calculations and measurements of this key chemical rate (see discussion by Florescu-Mitchell & Mitchell 2006 and references therein). In Sect. 7 we discuss the influence of adopting a smaller, “non standard” $\alpha'(\text{HCO}^+)$ rate on our results.

4.2. HOC^+ and H^{13}CO^+ chemistry in the PDR

In order to extract the $[\text{HOC}^+]$ and $[\text{H}^{13}\text{CO}^+]$ abundances towards the Horsehead PDR, we have modeled the observed lines (Fig. 2) using our best knowledge of the prevailing physical conditions: $T_k = 60\text{--}120$ K, $n(\text{H}_2) = 5 \times 10^4 \text{ cm}^{-3}$, $n(\text{H}) = 500 \text{ cm}^{-3}$, $[e^-] = 5 \times 10^{-5}$ and a 0.1 pc line-of-sight depth (or $N_H \approx 3.1 \times 10^{22} \text{ cm}^{-2}$) all accurate within a factor ~ 2 . From the observed lines we derive the following column densities: $N(\text{HOC}^+) = (1.2\text{--}2.5) \times 10^{11} \text{ cm}^{-2}$ and $N(\text{H}^{13}\text{CO}^+) = (4.7\text{--}7.8) \times 10^{11} \text{ cm}^{-2}$, which translates into $[\text{HOC}^+] = (0.4\text{--}0.8) \times 10^{-11}$ and $[\text{H}^{13}\text{CO}^+] = (1.5\text{--}2.5) \times 10^{-11}$. This computation assumes that the HOC^+ and H^{13}CO^+ emission fills the IRAM-30m beam. However, HOC^+ has not been mapped and its emission could well arise from the same $\sim 12''$ -width filament where the emission of small hydrocarbons and HCO radical is concentrated (Pety et al. 2005, Gerin et al. 2009). In this case, $[\text{HOC}^+]$ increases by a factor ~ 3 . Therefore, we conclude that the $[\text{HOC}^+]/[\text{H}^{13}\text{CO}^+]$ abundance ratio towards the PDR lies in the range $\approx 0.3\text{--}0.8$. These values are orders of magnitude higher than the value expected in the UV shielded gas.

Our chemical models (see next section) reproduce the $[\text{HOC}^+]/[\text{H}^{13}\text{CO}^+]$ abundance ratio towards the PDR but the absolute abundances derived from observations are larger than those predicted by the model. The discrepancies between observed and modeled abundances for HOC^+ and H^{13}CO^+ have likely a common origin. In particular, the formation of HOC^+ in UV irradiated gas is driven by reactions involving C^+ and species

such as H_2O and CO^+ (from $\text{C}^+ + \text{OH}$ reaction) that efficiently form at high temperatures, that is:



where reaction 7 predominantly produces HOC^+ whereas reaction 8 has similar branching ratios for the HCO^+ and HOC^+ formation (*e.g.*, Scott et al. 1997, Savage & Ziurys 2004). The HOC^+ destruction is governed by the isomerization reaction:



Laboratory experiments show that the reaction rate is smaller than previously thought (Smith et al. 2002), allowing interstellar HOC^+ to exist at detectable amounts.

The intensity peak of the $\text{CO } J=2\text{--}1$ optically thick lines observed with the PdBI ($T_{mb} \approx 60 \text{ K} \leq T_{ex}$; Pety et al. 2005), together with the observed $\text{CO } J=4\text{--}3/2\text{--}1$ line ratio (Philipp et al. 2006), provide a lower limit to the gas temperature in the PDR ($T_k \approx 60\text{--}120$ K). Temperatures in this range are predicted by the PDR model but are not enough to overcome the activation energy barriers of the neutral-neutral reactions leading to the formation of abundant H_2O , OH and CO^+ (*e.g.*, Neufeld et al. 1995, Cernicharo et al. 2006). Therefore, our models predict HOC^+ and H^{13}CO^+ abundances lower than observed because their precursor molecules have low abundances, and reactions 7 and 8 are not efficient enough.

We have computed that gas temperatures around ~ 350 K are needed to reproduce the observed HOC^+ and H^{13}CO^+ abundances in the PDR through the previous scheme (see Fig. 3). Our models of the Horsehead (low UV radiation field) include photoelectric heating from PAHs and grains but do not predict such a warm gas component even if the PAH abundance is significantly increased. However, we do not model the PDR gas dynamics and thus processes such as shock waves, driven by the expansion of the H II region that compress the cloud edge, may provide additional gas heating sources to trigger this *warm chemistry*. This reasoning is partially consistent with the non detection of CO^+ lines, at least at the sensitivity level of our long integration observation ($\text{rms} \sim 50$ mK in a 0.20 km s^{-1} velocity width channel or $[\text{CO}^+] \leq 5 \times 10^{-13}$).

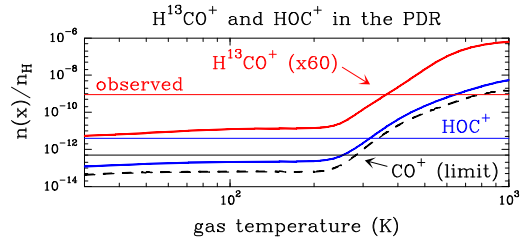


Fig. 3. Predicted H^{13}CO^+ , HOC^+ and CO^+ peak abundances in the PDR ($A_V \approx 0.5\text{--}1.5$) as a function of T_{gas} . H^{13}CO^+ and HOC^+ abundances (and CO^+ abundance upper limit) derived from observations towards the PDR are shown with horizontal thin lines.

If the gas in the PDR has not gone through such a *warm phase*, reaction 8 has to be ruled-out as the main chemical pathway for HOC^+ formation and an alternative formation scenario is required. In this case, we propose that the enhanced HOC^+ abundance in the PDR can still be related with the high abundance of C^+ (and thus high ionization fraction), but also with grain photodesorption of water-ice mantles formed in earlier evolutionary stages of the cloud.

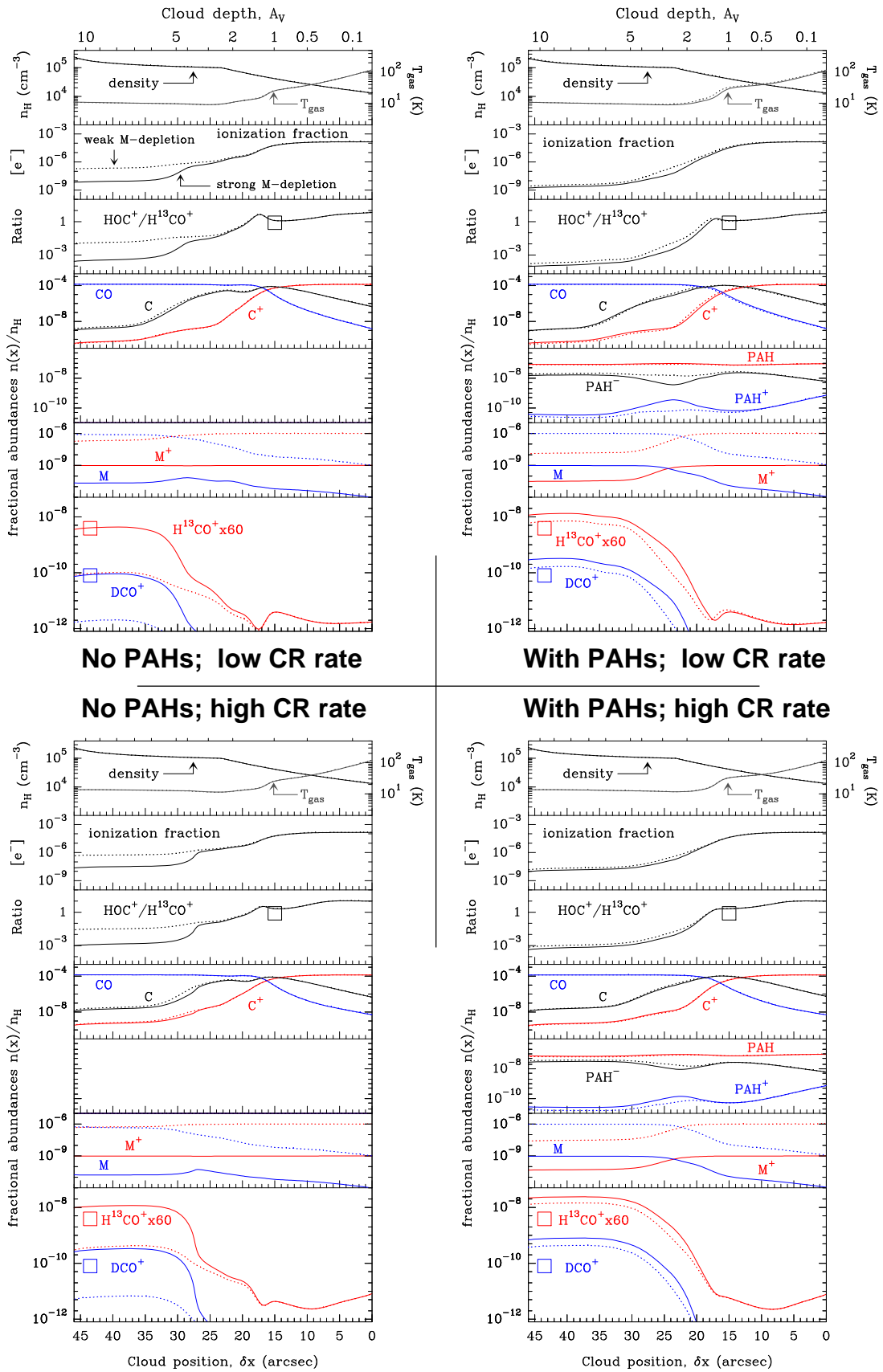


Fig. 4. Grid of chemical models for 2 different metal abundances, *low-metallicity* with $[M]=10^{-9}$ (*strong metal depletion case*, solid curves) and *high-metallicity* with $[M]=10^{-6}$ (*weak metal depletion case*, dashed curves). “Low CR rate” refers to models with $\zeta=3\times 10^{-17} \text{ s}^{-1}$ while models with “high CR rate” refer to $\zeta=3\times 10^{-16} \text{ s}^{-1}$. Models “with PAH” include PAH-gas interactions in the chemical network (with $[PAH]=10^{-7}$) while models with “no PAH” are pure gas-phase models. The black empty square represents the $[HOC^+]/[H^{13}CO^+]$ abundance ratio inferred towards the PDR from observations. The blue and red empty squares represent the DCO^+ and $H^{13}CO^+$ abundances derived towards the shielded core.

In this picture, the low χ/n ratio in the Horsehead ($\sim 10^{-3}$) will allow water-ices to be photodesorbed close to the illuminated edge of the cloud (see predictions by Hollenbach et al. 2009), increasing the water vapor abundance well above the pure-gas phase predictions. Reaction 7 will then dominate the HOC^+ formation in the PDR. Taking into account that isomerization, dissociative recombination and photodissociation contributes to HOC^+ destruction, we estimate that the required water vapor abundance needed to explain the inferred HOC^+ abundance in the PDR is $[\text{H}_2\text{O}] \approx 1800 \times [\text{HOC}^+] \approx (0.7-2.2) \times 10^{-8}$. *Herschel Space Observatory* observations will enable the detection of C^+ and H_2O lines in a large sample of PDRs, confirming whether or not water vapor is abundant at the *edges* of molecular clouds (e.g., Cernicharo et al. 2006).

5. Determination of the ionization fraction

Figure 4 presents depth-dependent predictions of several photochemical models across the Horsehead edge. Each model shows the main physical parameters (density and temperature), the ionization fraction gradient, the DCO^+ , H^{13}CO^+ and HOC^+ abundances (our observational probes of the ionization fraction) and the abundances of key chemical species for the charge balance in the cloud: $\text{CO}/\text{C}/\text{C}^+$, M/M^+ , $\text{PAH}^-/\text{PAH}/\text{PAH}^+$.

Four sets of models are displayed. *Top/bottom* models use a *low* ($\zeta = 3 \times 10^{-17} \text{ s}^{-1}$) and *high* ($\zeta = 3 \times 10^{-16} \text{ s}^{-1}$) cosmic-rays ionization rate respectively. *Left/right* models exclude and include the effects of PAHs respectively. In the latter case, we include PAHs in the UV radiative transfer (as a source of absorption and scattering of UV photons), in the photoelectric heating and in the chemical network. We start the chemistry computation by including neutral PAH alone with an initial abundance of $[\text{PAH}] = 10^{-7}$. In each set of models (each panel), the only parameter that varies is the abundance of metals: *high* metallicity with $[\text{M}] = 10^{-6}$ (dashed curves) and *low* metallicity with $[\text{M}] = 10^{-9}$ (solid curves). The low metallicity case implies a large metal depletion from the gas phase.

In terms of the chemical species observed in this work, a salient feature of all models is the constancy of the $\text{DCO}^+/\text{H}^{13}\text{CO}^+$ abundance ratio once the gas is shielded from UV radiation ($A_V \gtrsim 6$). This feature agrees with the almost identical spatial distribution of DCO^+ and H^{13}CO^+ emission observed beyond the PDR (see Fig. 1). This similarity was already noticed in the lower resolution DCO^+ and H^{13}CO^+ pioneering maps of several molecular clouds (e.g., Guélin et al. 1982). Besides, the predicted $[\text{HOC}^+]/[\text{H}^{13}\text{CO}^+]$ abundance ratio towards the PDR is in good agreement with the value inferred from observations. In this UV irradiated region where the C^+ and electron abundances are very high, the HCO^+ destruction rate becomes comparable to the isomerization rate (reaction 9). This implies that the $[\text{HOC}^+]/[\text{H}^{13}\text{CO}^+]$ abundance ratio in the cloud achieves the highest value in the PDR.

5.1. The role of ionized carbon and metals

According to the ionization fraction gradient all models show two differentiated environments separated by a transition region: the “PDR” ($A_V \approx 0-2$) and the “shielded core” ($A_V \gtrsim 6$). The electron density at every cloud position is given by the difference of cations and anions densities;

$$n_e = \sum_i n_i(\text{cations}^+) - \sum_j n_j(\text{anions}^-). \quad (10)$$

In the PDR, carbon, the most abundant heavy element with a ionization potential below 13.6 eV, provides most of the charge: $n(e^-) \approx n(\text{C}^+)$. Therefore, the ionization fraction in the PDR is high, $[e^-] \sim 10^{-4}$ (or $n_e \sim 1-5 \text{ cm}^{-3}$), and independent of elemental abundances other than carbon.

As A_V increases inwards the cloud, the C^+ abundance decreases by several orders of magnitude and so does the abundance of electrons. In the shielded core ($A_V \gtrsim 6$), low ionization heavy metal ions (e.g., Fe^+ , Mg^+ or Na^+) determine much of the ionization fraction (Oppenheimer & Dalgarno 1974, Guélin et al. 1982). In the absence of PAHs, abundant molecular ions m^+ transfer charge fast to heavy metal atoms M through $m^+ + M \rightarrow m + M^+$ reactions. Metal ions recombine orders of magnitude slower than molecular ions (Table 4), and thus a large fraction of them is kept ionized (higher $[\text{M}]$ implies higher electron abundances). Therefore, the ionization fraction in the core is highly dependent on the adopted metallicity, and varies from a few $\times 10^{-9}$ for $[\text{M}] = 10^{-9}$, to a few $\times 10^{-7}$ for $[\text{M}] = 10^{-6}$.

5.2. The role of PAHs

Depending on their abundances, the presence of PAHs can alter the chemistry and the ionization balance in dense clouds (e.g., Lepp & Dalgarno 1988). For our adopted abundance of $[\text{PAH}] = 10^{-7}$ the right and left panels in Fig. 4 shows that the presence of PAHs mostly modifies the ionization fraction at $A_V \gtrsim 2$. If not all PAHs accrete onto bigger grains or coagulate towards cloud interiors, PAH^- can be abundant through the cloud because the radiative electron attachment rate



is high ($\geq 10^{-7} \text{ cm}^3 \text{ s}^{-1}$), although probably dependent on the PAH size (Omont 1986, Allamandola et al. 1989, Flower et al. 2007, Wakelam & Herbst 2008). In the shielded core PAH^- is destroyed by recombination with atomic (M^+, \dots) and molecular cations (HCO^+ , $\text{H}_3\text{O}^+, \dots$) which are orders of magnitude less abundant than the available cations in the PDR (C^+ , S^+, \dots). Negative PAH ions thus reach high abundances ($[\text{PAH}^-] \approx 2 \times 10^{-8}$). For our choice of PAH parameters, this means that **PAH⁻ can be the most abundant negatively charged species, more than electrons for $A_V \geq 5$** . In addition, recombination of atomic ions on PAH^- is by far more efficient than the slow radiative recombination on electrons. This is a very important point since **heavy metal ions are now neutralized at similar rates than molecular ions**. As a result, both the abundance of metal cations and the ionization fraction decreases when PAHs are included, while molecular ions such as H^{13}CO^+ and DCO^+ increase their abundances (see Fig. 4 *right panels*).

In the illuminated edge of the cloud, PAH^- is predominantly destroyed by UV photons through electron detachment,



and through recombination with atomic cations which are very abundant in the PDR (e.g., Bakes & Tielens 1998, Wolfire et al. 2008). In consequence, the abundance of ions such as S^+ in the PDR decreases with respect to models without PAHs. This effect is important to determine the elemental abundances and depletion factors. Despite the higher PAH^- destruction rates in the PDR, the high electron density and relatively low UV field in the Horsehead allows PAH^- to form efficiently through electron attachment (reaction 11). Hence the resulting PAH^- abundance is also high in the PDR. On the other hand, the predicted abundance of positively charged PAH^+ in our models is ~ 500 times smaller than the abundance of PAH^- (due to

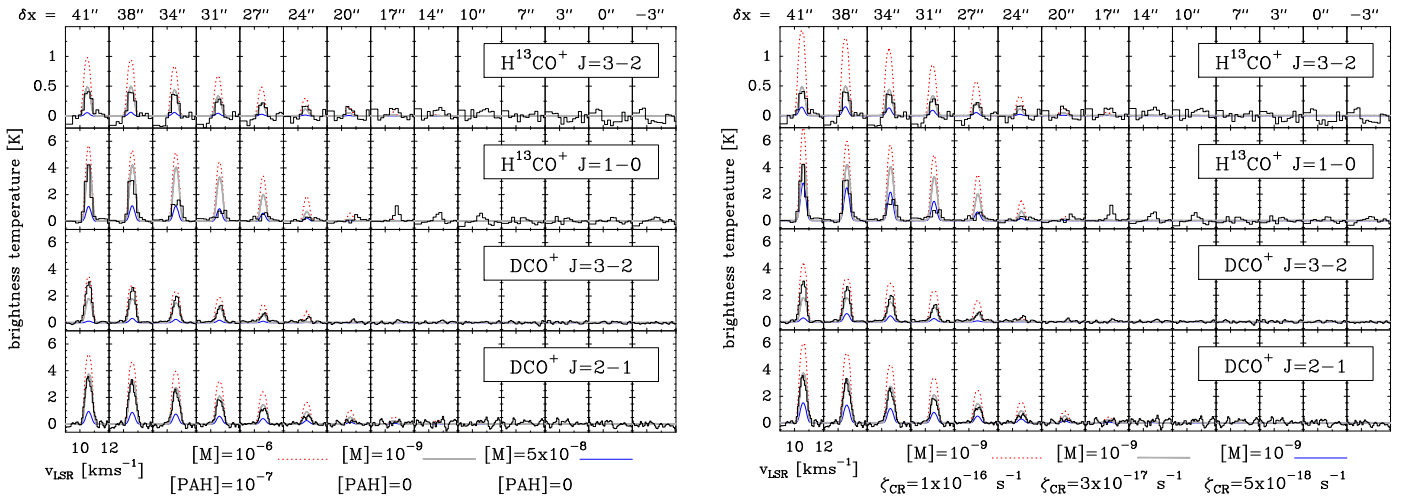


Fig. 5. *Left:* H^{13}CO^+ and DCO^+ spectra along the direction of the exciting star at $\delta y = 15''$ (histograms). Radiative transfer models using the output of PDR models for a fixed cosmic rays ionization rate ($\zeta = 3 \times 10^{-17} \text{ s}^{-1}$) and varying metallicities. *Thin blue curves* for $[\text{M}] = 5 \times 10^{-8}$ and no PAHs; *thick grey curves* for $[\text{M}] = 10^{-9}$ and no PAHs; and *dashed red curves* for $[\text{M}] = 10^{-6}$ and $[\text{PAH}] = 10^{-7}$. Modeled line profiles have been convolved with the appropriate Gaussian beam at each observed frequency (the angular resolution for each line are quoted in Tables 1 and 2). *Right:* Same as previous figure but for a fixed metal abundance ($[\text{M}] = 1 \times 10^{-9}$), no PAHs and varying cosmic rays ionization rate ζ . *Thin blue curves* for a model with $\zeta = 5 \times 10^{-18} \text{ s}^{-1}$; *thick grey curves* for $\zeta = 3 \times 10^{-17} \text{ s}^{-1}$; and *dashed red curves* for $\zeta = 10^{-16} \text{ s}^{-1}$.

fast electronic recombination) and therefore PAH^+ don't seem to play a major role in the ionization balance inside the cloud (see also Lepp & Dalgarno 1988, Wakelam & Herbst 2008).

5.3. The role of the cosmic-ray ionization rate

Cosmic rays affect the ionization state and the physics of molecular clouds, being the dominant source of heating and ionization in the gas shielded from interstellar radiation fields. Indeed, *secondary* UV photons are created in cloud interiors by H_2 electronic cascades following H_2 excitation by collisions with cosmic rays (Prasad & Tarafdar 1983). Therefore, cosmic rays maintain a certain ionization degree in the shielded gas and play a fundamental role in the ion-neutral chemistry by setting the abundance of key ions (Herbst & Klemperer 1973).

Most studies based on the interpretation of observed molecular ions set a range of a few 10^{-17} to a few 10^{-16} s^{-1} for the cosmic-ray ionization rate (Le Petit et al. 2004, van der Tak 2006, Dalgarno 2006 and references therein). However, it is still discussed whether or not ζ depends on environmental conditions (*e.g.*, galactic center vs. disk clouds) or if it varies from source to source (*e.g.*, from dense molecular cores to more translucent clouds). In many ways, PDRs offer an interesting intermediate medium to analyze the transition between translucent and dark clouds.

In terms of our observations, the DCO^+ and H^{13}CO^+ abundances directly scale with ζ in the UV shielded gas. Indeed, these ions are direct products of the H_3^+ destruction (through reactions 2 and 3), and the H_3^+ formation is proportional to $\approx \zeta n_{\text{H}}$. However, ζ and the metal abundance can not be constrained independently from the inferred DCO^+ and H^{13}CO^+ abundances since both parameters control the ionization fraction, and thus the destruction of these ions through reactions 5 and 6.

6. Results: observational constraints

In this section we compare the synthetic and observed H^{13}CO^+ and DCO^+ spectra as a function of cloud position. We then ex-

plore the range of metallicities and cosmic-rays ionization rates compatible with the H^{13}CO^+ and DCO^+ inferred abundances (see Table 6). The influence of PAHs is also investigated. We finally compare the $[\text{HOC}^+]/[\text{H}^{13}\text{CO}^+]$ ratio obtained towards the Horsehead with the values derived in other PDRs.

6.1. Constraints to the metals abundance

Figure 5 *left* shows the spectra along the direction of the exciting star (histograms) and radiative transfer models using the output of several PDR models for a fixed ionization rate ($\zeta = 3 \times 10^{-17} \text{ s}^{-1}$) and varying metallicities. In particular, the model with $[\text{M}] = 10^{-9}$ (and no PAHs) displays a notable agreement with both the DCO^+ and H^{13}CO^+ spatial distribution and with the inferred peak abundances towards the core (Table 6). In addition, Fig. 6 *left* shows the predicted ionization fraction and $[\text{H}^{13}\text{CO}^+]$ and $[\text{DCO}^+]$ abundances at the core peak ($A_V > 10$) as a function of $[\text{M}]$ (blue-solid curves). These models (no PAHs, fixed ζ) shows that the **upper limit metallicity compatible with observations is $[\text{M}] \leq 4 \times 10^{-9}$, which implies a ionization fraction of $[e^-] = (7 \pm 1) \times 10^{-9}$ at the core peak.** Higher metal abundances increase the ionization fraction (see Fig. 6 *left*), which translates into weaker lines than observed (Fig. 5 *left*: blue-thin curves). Therefore, the gas-phase metal abundance is depleted by ~ 4 orders of magnitude with respect to the Sun ($[\text{M}] \approx 8.5 \times 10^{-5}$; Anders & Grevesse 1989). This range of depletion is similar to that obtained in other prestellar cores such as Barnard 68 (Maret & Bergin 2007). We shall refer it as the *strong metal depletion* case.

The inclusion of PAH interactions implies lower ionization fractions and enhanced molecular ion abundances (see Fig. 6 *left*) which results in overestimated H^{13}CO^+ and DCO^+ line intensities towards the core. Therefore, the abundance of metals (*e.g.*, the ionization fraction indirectly) has to be increased to match the observed intensities. In particular, Fig. 5 *left* shows that a model with $[\text{PAHs}] = 10^{-7}$ and $[\text{M}] = 10^{-6}$ (red-dashed curves) displays only a factor < 2 brighter lines than models with 3 orders of magnitude lower metallicities and no

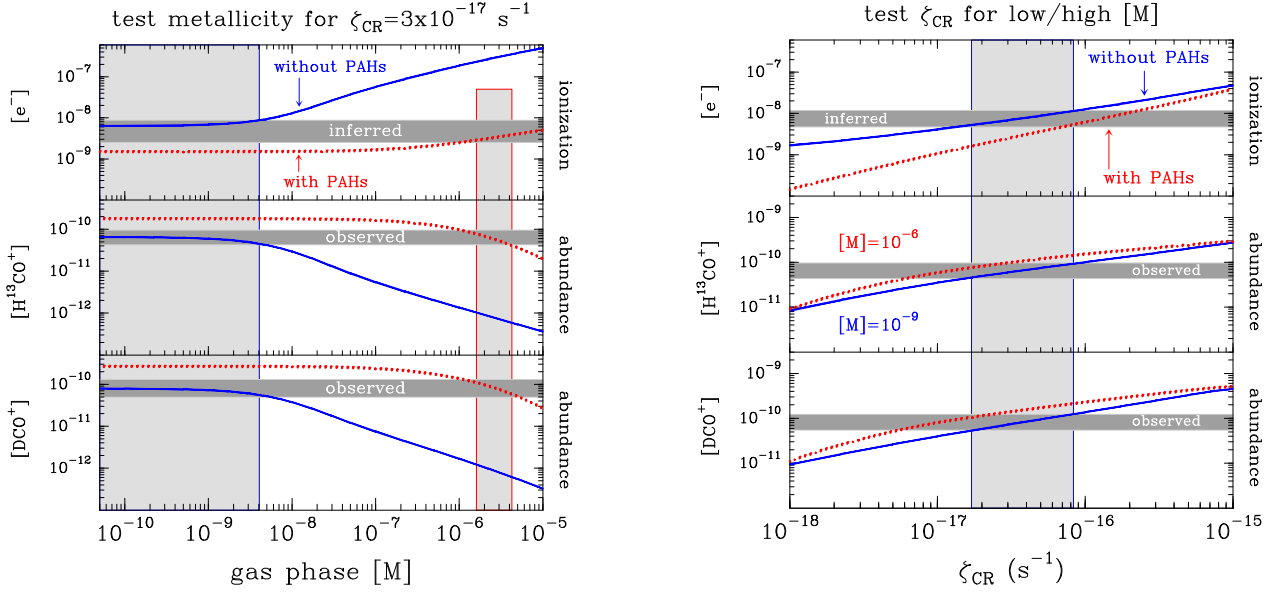


Fig. 6. *Left:* Model predictions for the shielded core (the “DCO⁺ peak” at $A_V > 10$). The ionization rate due to cosmic rays is fixed to $\zeta = 3 \times 10^{-17} \text{ s}^{-1}$. The different panels show (*upper*): the ionization fraction, (*middle*): the H^{13}CO^+ abundance and (*lower*): the DCO^+ abundance as a function of gas phase metallicity. Blue-solid curves for models without PAHs, and red-dotted curves for models with neutral and charged PAHs ($[\text{PAH}] = 10^{-7}$). Horizontal shaded regions show the H^{13}CO^+ and DCO^+ abundances derived from observations towards the core, while vertical shaded regions show the parameter space compatible with observations. *Right:* Same as previous figure but for a fixed low metallicity of $[\text{M}] = 10^{-9}$ (no PAH; blue-solid curves) and a fixed high metallicity of $[\text{M}] = 10^{-6}$ ($[\text{PAH}] = 10^{-7}$; red-dotted curves). The different panels show (*upper*): the ionization fraction, (*middle*): the H^{13}CO^+ abundance and (*lower*): the DCO^+ abundance as a function of the ionization rate due to cosmic rays.

Table 6. Inferred abundances $[x] = N(x)/N_{\text{H}}$ where $N_{\text{H}} = N(\text{H}) + 2N(\text{H}_2)$.

Species	shielded core $A_V \geq 6$ $\delta x \approx 45''$	PDR $A_V = 0-2$ $\delta x \approx 15''$
$N_{\text{H}} (\text{cm}^{-2})$	5.8×10^{22}	3.1×10^{22}
$[\text{H}^{13}\text{CO}^+]$	6.5×10^{-11}	1.5×10^{-11}
$[\text{H}^{12}\text{CO}^+]$	3.9×10^{-9}	9.0×10^{-10}
$[\text{DCO}^+]$	8.0×10^{-11}	(-)
$[\text{HOC}^+]$	(-)	$0.4 \times 10^{-11} \dagger$
$[\text{CO}^+]$	(-)	$\leq 5.0 \times 10^{-13}$
$[e^-]$	$(1 - 8) \times 10^{-9}$	$10^{-6} - 10^{-4}$

\dagger Assuming extended emission. It would be 1.2×10^{-11} if HOC^+ arises from a $12''$ -width filament as HCO (Gerin et al. 2009).

PAHs (grey-thick curves). As shown in Fig. 6 left, the inclusion of PAHs makes the range of metal abundances compatible with observations much higher now, $[\text{M}] = (3 \pm 1) \times 10^{-6}$. The required abundance of metals is at least a factor ~ 500 larger than the former case without PAHs. Thus, we refer it as the *weak metal depletion* case. Note that this metallicity is still below the gas-phase abundance of Fe+Mg+... elements in the diffuse interstellar gas (e.g., Wolfire et al. 1995, Howk et al. 2006) and is consistent with the incorporation of metals into dust grains in higher density regions (e.g., Wolfire et al. 1995). On the other hand, the ionization fraction required to reproduce the H^{13}CO^+ and DCO^+ abundances does not change much, $[e^-] = (4 \pm 1) \times 10^{-9}$ at the core peak (red-dashed curves Fig. 6 left). Therefore, it is not easy to distinguish between the *strong metal depletion* (no PAHs) and *weak metal depletion* (with PAHs) cases in terms of the ionization fraction. The observation of forbidden lines from metals such as $[\text{Fe II}]$ towards the UV illuminated edges of

molecular clouds may help to remove this apparent degeneracy. In one of the few positive cases, the S140 PDR, the detection of a weak $[\text{Fe II}] 26.0 \mu\text{m}$ fine-structure line emission suggests that iron is depleted, but with an abundance of $\sim 5 \times 10^{-8}$ relative to H (Timmermann et al. 1996). Nevertheless, without mapping and comparing with other PDR tracers, it is not obvious to disentangle whether $[\text{Fe II}]$ lines arise from the PDR gas or from the adjacent (HII) ionization front (e.g., Marconi et al. 1998, Kaufman et al. 2006).

6.2. Constraints to the cosmic-ray ionization rate

Figure 5 right shows again the observed spectra along the direction of the exciting star (histograms) and radiative transfer models using the output of PDR models that vary the cosmic rays rate, without PAHs and a fixed metal abundance of $[\text{M}] = 10^{-9}$. The adopted metal abundance is, within an order of magnitude, the usual value estimated in prestellar cores (e.g., Caselli et al. 1999, Maret & Bergin 2007) and is compatible with our *strong metal depletion case*. Therefore, Fig. 5 right shows the effects of different ionization rates directly on the DCO^+ and H^{13}CO^+ line intensities. For the adopted physical conditions and chemical network, our observations constrain ζ within a factor ~ 2 . In particular, Fig. 6 right shows the predicted $[e^-]$, $[\text{H}^{13}\text{CO}^+]$ and $[\text{DCO}^+]$ abundances at the core peak ($A_V > 10$) as a function of ζ , and evidences that in the absence of PAHs, the cosmic rays ionization rate range compatible with the observations of the Horsehead edge is $\zeta = (5 \pm 3) \times 10^{-17} \text{ s}^{-1}$ (blue-solid curves). If PAHs are included in the chemistry, the metal abundance has to be increased accordingly to reproduce the observations. For our $[\text{PAH}] = 10^{-7}$ model case, the required metal abundance needs to be above $[\text{M}] \approx 10^{-6}$ to obtain ionization rates above $\zeta \approx 10^{-17} \text{ s}^{-1}$ (Fig. 6 right; red-dotted curves).

Note that given the fact that the H^{13}CO^+ formation in the PDR is not dominated by the $^{13}\text{CO} + \text{H}_3^+$ reaction, the H^{13}CO^+ abundance in the UV illuminated gas does not scale with ζ . Therefore, we can not further investigate if ζ varies significantly in the transition from diffuse regions to the shielded core (e.g., McCall et al. 2003, Padoan & Scalo 2005).

6.3. High ionization fraction in the PDR

The bright $[\text{C II}]158\mu\text{m}$ (Zhou et al. 1993) and $[\text{C I}]492\text{ GHz}$ (Philipp et al. 2006) fine structure line emission towards the Horsehead PDR, together with subtle chemical effects such as the large $[l\text{-C}_3\text{H}_2]/[c\text{-C}_3\text{H}_2]$ linear-to-cyclic abundance ratio (Teyssier et al. 2005) all show observationally that the ionization fraction is higher in the UV illuminated edge than towards the cloud interior. Nevertheless, all those studies lacked the angular resolution to properly measure the ionization fraction gradient.

The abundances of reactive ions such as HOC^+ are also predicted to be enhanced in the UV illuminated gas, where we have shown that the ionization fraction is high, up to $[e^-] \sim 10^{-4}$, and that the HOC^+ formation is linked to the availability of C^+ . On the other hand, the H^{13}CO^+ abundance increases as the electron abundance decreases towards the shielded core. Therefore, we predict that **the $[\text{HOC}^+]/[\text{H}^{13}\text{CO}^+]$ abundance ratio scales with the ionization fraction gradient**, reaching the highest values in the PDR (Fig. 4). In particular, we derive a high $[\text{HOC}^+]/[\text{H}^{13}\text{CO}^+] = 0.3\text{--}0.8$ ratio (or a low $[\text{HCO}^+]/[\text{HOC}^+] \approx 75\text{--}200$ ratio) towards the PDR, similar to that observed in other PDRs such as NGC7023 (Fuente et al. 2003).

7. Discussion

7.1. The ionization fraction gradient

Star forming clouds display different environments depending on the dominant physical and chemical processes. These environments are, in a first approximation, similar to those studied here: (i) a low density *cloud edge* directly exposed to a UV radiation field from nearby stars; (ii) a *transition region* or *ridge* where the H_2 density increases as the gas temperature decreases due to the attenuation of the external radiation field. UV photons can still play a significant role depending on their penetration depths (e.g., cloud clumpiness, grain properties, etc.) and (iii) the denser *shielded cores* that may be externally triggered to form a new generation of stars depending on their stability against gravitational collapse (e.g., Goicoechea et al. 2008).

Assuming that the observed field-of-view in the Horsehead nebula is representative of the above 3 environments, our maps and chemical models reveal that **the ionization fraction follows a steep gradient in molecular clouds**: from $[e^-] \approx 10^{-4}$ at the *edge* of the cloud (the “ C^+ dominated” region) to a few times $\sim 10^{-9}$ in the *shielded cores*. The prevailing chemistry and the abundance of atomic ions such as C^+ and S^+ determine the “slope” of the ionization fraction gradient in the *transition* regions. In particular, sulfur (with a ionization potential of $\sim 10.36\text{ eV}$) is a good source of charge behind the “ C^+ dominated” region. Advection and time-dependent effects may also modify the ionization fraction gradient with time. However, Morata & Herbst (2008) have shown models for (uniform) physical conditions similar to those in the Horsehead where $[\text{HCO}^+]$ (and $[e^-]$ presumably) does not change with time appreciably.

Figure 7 shows the predicted ionization fraction gradient, with a scale length of $\sim 0.05\text{ pc}$ (or $\sim 25''$), and the main charge carriers for 3 representative models with fixed *stan-*

ard metal abundance (our *strong metal depletion case*) and *standard* cosmic-ray rate. Panel 7a shows a model without PAHs and high gas-phase sulfur abundance ($[\text{S}] = 3.5 \times 10^{-6}$; Goicoechea et al. 2006). The ionization fraction gradient in the *core/transition/edge* zones, is mainly determined by the $[\text{HCO}^+ + \text{S}^+ + \text{M}^+ + \dots]/[\text{S}^+]/[\text{C}^+]$ abundances respectively. Sulfur ions control the charge balance in the *transition* layers, and due to their high abundance and slow radiative recombination rate with electrons, the ionization fraction is high, a few times 10^{-7} , and the gradient is smooth. This model qualitatively agrees with the observed more extended emission and narrower line-widths of sulfur recombination lines compared to carbon recombination lines in dark clouds, as well as with the relatively low (< 10) carbon-to-sulfur recombination lines intensity ratio (e.g., Pankonin & Walmsley 1978, Falgarone et al. 1978). All these signatures argue in favor of extended regions with significant amounts of gas-phase S^+ .

Panel 7b shows the same model but sulfur abundances smaller by two orders of magnitude (strong gas-phase sulfur depletion). The ionization fraction in the cloud *core* ($A_V > 6$) and *edge* ($A_V < 2$) are nearly the same as in the previous high sulfur abundance model. However, the lack of abundant S^+ in the *transition* layers decreases the electron abundance considerably, and makes the ionization fraction gradient much steeper. Observational constraints to the atomic and ionic S abundances from far-IR fine structure lines or recombination lines, and a careful treatment of the sulfur chemistry (i.e., which are the most abundant S-bearing species as a function of cloud depth?) are thus required to quantify the S^+ abundance at large A_V and its impact on the charge balance.

Panel 7c finally shows a model with high sulfur abundance again but including PAHs (with $[\text{PAH}] = 10^{-7}$). As presented in Sect. 5.2, negatively charged PAH^- efficiently form by radiative electron attachment and their abundance remains high through the cloud. Given the much higher recombination rates of atomic ions on PAH^- than on electrons, the abundance of atomic ions such as S^+ in the *transition zone*, or M^+ in the *shielded cores*, quickly decreases. Hence, lower ionization fractions (and a much weaker dependence on the assumed metal elemental abundance) are predicted by the model with PAHs. This results agrees with theoretical predictions for UV shielded gas (Lepp & Dalgarno 1988, Flower et al. 2007, Wakelam & Herbst 2008).

In summary, a high abundance of PAHs *throughout* the molecular cloud (not only in the PDR) plays a role in the ionization balance and in the abundance of molecular ions, which affects the determination of elemental abundances (e.g., S) from fractional molecular abundances (e.g., HCS^+/CS , SO^+/SO , etc.).

7.2. The PAH abundance in UV shielded gas

The PAH abundance in the dense and UV shielded gas is far from being well constrained. Different approaches to analyze ISO and *Spitzer* mid-IR observations towards several PDRs all argue in favor of an evolution of dust grain sizes: from the illuminated cloud edge where the emission of PAH bands dominates, to the shielded interiors where the continuum emission from bigger grains dominates (Rapacioli et al. 2005, Berné et al. 2007, Compiègne et al. 2008). It is not trivial to disentangle whether this is a physical effect (i.e., free PAHs are not present in the shielded regions) or an excitation effect (i.e., lack of UV photons). Even if the PAH abundance drastically decrease towards cloud interiors, a chemically significant fraction of them may survive. Unfortunately, while the effects

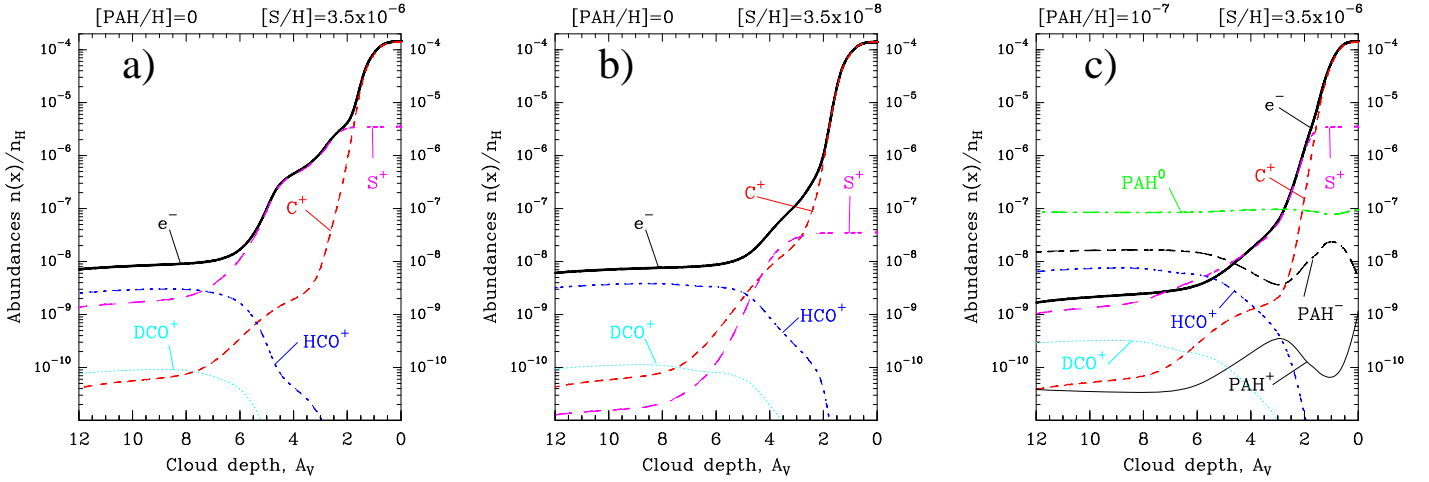


Fig. 7. Derived abundance profiles for the most significant ions studied in this work for different PAH and sulfur elemental abundances. An enhanced UV radiation field 60 times the mean ISRF illuminates the cloud from the right. The metal abundance ($[M]=10^{-9}$) and the cosmic-ray rate ($\zeta=3\times 10^{-17}\text{ s}^{-1}$) are fixed in all models. *a)* Model with $[PAH]=0$ and $[S]=3.5\times 10^{-6}$ (low sulfur depletion). *b)* Model with $[PAH]=0$ and $[S]=3.5\times 10^{-8}$ (high sulfur depletion). *c)* Model with $[PAH]=10^{-7}$ and $[S]=3.5\times 10^{-6}$.

of grain growth in the UV extinction curve have been modelled by us (Goicoechea & Le Bourlot 2007), including PAH coagulation/accretion in the chemistry is beyond the scope of this work. All we can say at this point is that a better description of the cloud chemistry may be a decreasing PAH abundance gradient or an increasing PAH size distribution towards the cloud interior. In any case, we have shown that the presence of free PAHs in molecular clouds modifies the prevailing chemistry. As a result, the predicted high abundance of PAH^- can dominate the recombination of metal ions and reduce the ionization fraction.

The presence of abundant free PAHs, or large molecules to which electron attach (Lepp & Dalgarno 1988), can thus be crucial in determining the coupling of the gas with magnetic fields in molecular clouds, but also in collapsing cores or in the “dead” zones of protoplanetary disks (magnetically inactive regions where accretion can not occur if the ionization fraction is very low). According to our models, **the PAH abundance threshold required to affect the metal and electron abundance determination in the UV shielded gas is $[PAH]>10^{-8}$** . *Herschel* observations might allow the identification of specific PAH carriers through their far-IR skeletal modes (Joblin et al. 2002; Mulas et al. 2006), thus providing clues on their composition and abundance variations in different environments.

7.3. “Non standard” HCO^+ dissociative recombination rate

We conclude by discussing the sensitivity of our determination of the ionization fraction from $H^{13}CO^+$ and DCO^+ abundances. In particular, we have checked the effects of adopting a smaller, “non standard” HCO^+ dissociative recombination rate, $\alpha'(HCO^+)=0.7\times 10^{-7}(300/T)^{0.50}\text{ cm}^3\text{ s}^{-1}$ (Sheehan 2000, Florescu-Mitchell & Mitchell 2006). For models without PAHs, the predicted $H^{13}CO^+$ and DCO^+ abundances increase by a factor ~ 3 with respect to models using the “standard” $\alpha(HCO^+)$ rate (Table 4), but the metallicity required to fit the observed lines has to be increased to $[M]\approx 5\times 10^{-8}$ and the predicted ionization fraction increases to $[e^-]\approx 5\times 10^{-8}$ in the core. This value should be regarded as the upper limit of our determination. On the other hand, the influence of $\alpha'(HCO^+)$ in models with PAHs is less important. It also requires high metallicities to fit the ob-

served intensities (*weak metal depletion* case), but the predicted $[e^-]$ in the shielded core remains low (below $\sim 10^{-8}$).

8. Summary and conclusions

We have presented the first detection of HOC^+ reactive ion towards the Horsehead PDR. Combined with our previous IRAM-PdBI $H^{13}CO^+$ $J=1-0$ (Gerin et al. 2009) and IRAM-30m $H^{13}CO^+$ and DCO^+ higher- J line maps (Pety et al. 2007) we performed a detailed analysis of their chemistry, excitation and radiative transfer to constrain the ionization fraction as a function of cloud position. The observed field contains 3 different environments: (i) the UV illuminated *cloud edge*, (ii) a *transition* region or *ridge* and (iii) a dense and cold shielded *core*. We have presented a study of the ionization fraction gradient in the above environments, which can be considered as templates for most molecular clouds. Our main conclusions are the following:

1. The ionization fraction follows a steep gradient, with a scale length of $\sim 0.05\text{ pc}$ ($\sim 25''$), from $[e^-]\approx 10^{-4}$ ($n_e\sim 1-5\text{ cm}^{-3}$) at the *cloud edge* (the “ C^+ dominated” regions) to a few times $\sim 10^{-9}$ in the *shielded core* (with ongoing deuterium fractionation). Sulfur, metal and PAH ions play a key role in the charge balance at different cloud depths.
2. The detection of HOC^+ towards the PDR, and the high $[HOC^+]/[H^{13}CO^+]\approx 0.3-0.8$ abundance ratio inferred, proves the high ionization fraction in the UV irradiated gas. However, the $H^{13}CO^+$ and HOC^+ abundances derived from observations are larger than the PDR model predictions. We propose that either the gas is/was warmer than predicted or that significant water ice-mantle photodesorption is taking place and HOC^+ is mainly formed by the $C^+ + H_2O$ reaction.
3. The ionization fraction in the shielded core depends on the metal abundance and on the cosmic-rays ionization rate. Assuming a *standard* rate of $\zeta=3\times 10^{-17}\text{ s}^{-1}$ and pure gas-phase chemistry (no PAHs), the metal abundance has to be lower than 4×10^{-9} (strong metal depletion). Conversely, assuming a *standard* metal abundance of $[M]=10^{-9}$, our observations can only be reproduced with $\zeta=(5\pm 3)\times 10^{-17}\text{ s}^{-1}$.
4. The inclusion of PAHs modifies the ionization fraction gradient and decreases the metal depletion required to reproduce

the observations if $[PAH] > 10^{-8}$ (*i.e.*, if not all PAHs coagulate/accrete onto bigger grains). In such a case, PAH^- acquire large abundances also in the shielded gas. Recombination of atomic ions on PAH^- is much more efficient than on electrons and thus metal ions are neutralized at similar rates than molecular ions. For $[PAH]=10^{-7}$, the metal abundance consistent with observations increases to $[M]=(3\pm 1)\times 10^{-6}$ (still below the heavy metals abundance in the diffuse ISM).

Acknowledgements. We thank the IRAM staff for their support during observations and D. Talbi and B. Godard for useful advice regarding the HCO^+ dissociative recombination rate. Inelastic collisional rates of HCO^+ with electrons were kindly provided by A. Faure and J. Tennyson. We also thank M. Walmsley for several interesting comments. We acknowledge the use of *OSU* (<http://www.physics.ohio-state.edu/~eric/research.html>) and *UDFA* (<http://www.udfa.net/>) chemical reaction data bases. We finally acknowledge financial support from CNRS/INSU research programme PCMI. JRG is supported by a *Ramón y Cajal* research contract from the Spanish MICINN and co-financed by the European Social Fund.

References

- Abergel, A., Teyssier, D., Bernard, J. P et al. 2003, *A&A*, 410, 577.
 Allamandola, L. J., Tielens, A. G. G. M. & Barker, J. R. 1985, *ApJ*, 290, L25.
 Allamandola, L. J., Tielens, A. G. G. M. & Barker, J. R. 1989, *ApJS*, 71, 733.
 Anders, E., & Grevesse, N. 1989, *Geochimica et Cosmochimica Acta*, 53, 197-214.
 Bakes, E. L. O. & Tielens, A. G. G. M. 1994, *ApJ*, 427, 822.
 Bakes, E. L. O. & Tielens, A. G. G. M. 1998, *ApJ*, 499, 258.
 Balbus, S.A. & Hawley, J.F. 1991, *ApJ*, 376, 214.
 Berné, O., Joblin, C., Deville, Y. et al. 2007, *A&A*, 469, 575.
 Boulanger, F., Falgarone, E., Puget, J. L. & Helou, G. 1990, *ApJ*, 364, 136.
 Caselli, P., Walmsley, C. M., Terzieva, R. & Herbst, E. 1998, *ApJ*, 499, 234.
 Caselli, P., Walmsley, C. M., Tafalla, M., Dore, L. & Myers, P. C. 1999, *ApJ*, 523, L165.
 Cernicharo, J. & Guélin, M. 1987, *A&A*, 176, 299.
 Cernicharo, J., Goicoechea, J.R., Pardo, J.R. & Asensio-Ramos, A. 2006, *ApJ*, 642, 940.
 Compiègne M., Abergel, A., Verstraete, L. et al. 2007, *A&A*, 471, 205.
 Compiègne M., Abergel, A., Verstraete, L. & Habart, E. 2008, *A&A*, 491, 797.
 Dalgarno, A. 2006, *Proceedings of the National Academy of Science*, 103, 33, 12269.
 de Boisanger, C., Helmich, F. P. & van Dishoeck, E. F. 1996, *A&A*, 310, 315.
 Desert, F.-X., Boulanger, F., & Puget, J. L. 1990, *A&A*, 237, 215.
 Falgarone, E., Cesarsky, D. A., Encrenaz, P. J. & Lucas, R. 1978, *A&A*, 65, L13.
 Faure, A. & Tennyson, J. 2001, *MNRAS*, 325, 443.
 Florescu-Mitchell, A.I. & Mitchell, J.B.A. 2006, *Physics Reports*, 430, 277
 Flower, D.R. 1999, *MNRAS*, 305, 651
 Flower, D.R. & Pineau des Forêts, G. 2003, *MNRAS*, 343, 390.
 Flower, D.R., Pineau des Forêts, G. & Walmsley, C. M. 2007, *A&A*, 474, 923.
 Fuente, A., Rodríguez-Franco, A., García-Burillo, S., Martín-Pintado, J., & Black, J. H. 2003, *A&A*, 406, 899.
 Fuente, A., García-Burillo, S., Usero, A. et al. 2008, *A&A*, 492, 675.
 Gerin, M., Goicoechea, J.R., Pety, J. & Hily-Blant, P. 2009, *A&A*, 494, 977.
 Gerlich, D., Herbst, E., & Roueff, E., 2002, *Planetary and Space Science*, 50, 12-13, 1275.
 Goicoechea, J. R., Pety, J., Gerin, M., Teyssier, D., Roueff, E., Hily-Blant, P. & Baek, S. 2006, *A&A*, 456, 565.
 Goicoechea, J. R. & Le Bourlot, J. 2007, *A&A*, 467, 1.
 Goicoechea, J. R., Berné, O., Gerin, M., Joblin, C. & Teyssier, D. 2008, *ApJ*, 680, 466.
 Graedel, T. E., Langer, W. D., & Frerking, M. A. 1982, *ApJS*, 48, 321.
 Greve, A., Kramer, C. & Wild, W. 1998, *A&AS*, 133, 271.
 Guélin, M., Langer, W. D. & Wilson, R. W. 1982, *A&A*, 1982, 107, 107.
 Habart, E., Abergel, A., Walmsley, C. M., Teyssier, D. & Pety, J. 2005, *A&A*, 437, 177.
 Herbst, E. & Klempner, W. 1973, *ApJ*, 185, 505.
 Hezareh, T. Houde, M., McCoey, C., Vastel, C. & Peng, R. 2008, *ApJ*, 684, 1221.
 Hily-Blant, P., Teyssier, D., Philipp, S. & Güsten, R. 2005, *A&A*, 440, 909.
 Hollenbach, D., Kaufman, M.J., Bergin, E.A. & Melnick, G.J. 2009, *ApJ*, 690, 1497.
 Howk, J.C., Sembach, K.R. & Savage, B.D. 2006, *ApJ*, 637, 333.
 Joblin, C., Toubanc, D., Boissel, P. & Tielens, A. G. G. M. 2002, *Mol.Phys.*, 100, 3595.
 Kaufman, M.J., Wolfire, M.G. & Hollenbach, D.J. 2006, *ApJ*, 644, 28.
 Langer, W. D., Graedel, T. E., Frerking, M. A. & Armentrout, P. B. 1984, *A&A*, 277, 581.
 Langer, W. D. & Penzias, A.A. 1990, *ApJ*, 357, 477
 Laor, A., & Draine, B.T. 1993, 402, 441
 Le Bourlot, J., Pineau Des Forets, G., Roueff, E., & Flower, D. R. 1993, *A&A*, 267, 233
 Leger, A. & Puget, J. L. 1984, *A&A*, 137, L5.
 Le Petit, F., Roueff, E., & Herbst, E. 2004, *A&A*, 417, 993.
 Le Petit, F., Nehmé, C, Le Bourlot, J. & Roueff, E. 2006, *ApJS*, 64, 506.
 Lepp, S. & Dalgarno, A. 1988, *ApJ*, 324, 553.
 Li, A. & Draine, B. T. 2001, *ApJ*, 554, 778.
 Liszt, H., Lucas, R., & Black, J. H. 2004, *A&A*, 428, 117L.
 Marconi, A., Testi, L., Natta, A. & Walmsley, C. M. 1998, *A&A*, 330, 696.
 Maret, S. & Bergin, E.A. 2007, *ApJ*, 664, 956.
 Mathis, J. S., Rumpl, W. & Nordsieck, K. H. 1977, *ApJ*, 217, 425
 McCall, B. J. et al. 2003, 2003, *Nature*, 422, 500.
 Morata, O. & Herbst, E. 2008, *MNRAS*, 390, 1549.
 Mulas, G., Mallocci, G., Joblin, C. & Toubanc, D. 2006, *A&A*, 460, 93.
 Neufeld, D.A., Lepp, S., & Melnick, G.J. 1995, *ApJS*, 100, 132.
 Omont, A., 1986, *A&A*, 164, 159
 Oppenheimer, M. & Dalgarno, A. 1974, *ApJ*, 192, 29.
 Padoan, P. & Scalo, J. 2005, *ApJ*, 624, L97
 Pankonin, V. & Walmsley, C. M. 1978, *A&A*, 67, 12.
 Penzias, A.A. & Burrus, C.A. 1973, *ARA&A*, 11, 51.
 Pety, J., Teyssier, D., Fossé, D., Gerin, M., Roueff, E., Abergel, A., Habart, E. & Cernicharo, J. 2005, *A&A*, 435, 885.
 Pety, J. SF2A-2005: Semaine de l'Astrophysique Française, meeting held in Strasbourg, France, 2005, Edited by F. Casoli, T. Contini, J.M. Hameury and L. Paganì. Published by EdP-Sciences, Conference Series, 2005, p. 721.
 Pety, J., Goicoechea, J. R., Hily-Blant, P., Gerin, M. Teyssier, D. 2007, *A&A*, 464, L41
 Philipp, S. D., Lis, D. C., Güsten, R., Kasemann, C., Klein, T. & Phillips, T. G. 2006, *A&A*, 454, 213.
 Prasad, S. S. & Tarafdar, S. P. 1983, *ApJ*, 267, 603.
 Rapacioli, M., Joblin, C., Boissel, P. 2005, *A&A*, 429, 193.
 Rapacioli, M., Calvo, F., Joblin, C., Parneix, P., Toubanc, D. and Spiegelman, F. 2006, *A&A*, 460, 519.
 Rizzo, J. R., Fuente, A., Rodríguez-Franco, A., García-Burillo, S. 2003, *ApJ*, 597, L153.
 Röllig, M., Abel, N. P., Bell, T. et al. 2007, *A&A*, 467, 187.
 Savage, C., Apponi, A. J., Ziurys, L. M. & Wyckoff, S. 2000, *ApJ*, 578, 211.
 Savage, C. & Ziurys, L. M. 2004, *ApJ*, 616, 966.
 Scott, G. B. I., Fairley, D. A., Freeman, C. G., McEwan, M. J., Spanel, P. & Smith, D. 1997, *J. Chem. Phys.*, 106, 3982-3987.
 Sheehan, C.H., 2000 *A merged beam analysis of the dissociative recombination of molecular ions of importance to ionospheric and interstellar chemistry*. Ph.D. thesis, The University of Western Ontario, London, Canada.
 Smith, M. A., Schlemmer, S., von Richthofen, J. & Gerlich, D. 2002, *ApJ*, 578, L87.
 Teyssier, D., Fossé, D., Gerin, M., Pety, J., Abergel, A. & Roueff, E. 2004, *A&A*, 417, 135.
 Teyssier, D., Hily-Blant, P., Gerin, M., Cernicharo, J., Roueff, E. & Pety, J. 2005, In: *Proceedings of the dusty and molecular universe: a prelude to Herschel and ALMA*, Ed. by A. Wilson. ESA SP-577, Noordwijk, Netherlands: ESA Publications Division, ISBN 92-9092-855-7, 423.
 Timmermann, R., Bertoldi, F., Wright, C. M., Drapatz, S., Draine, B. T., Haser, L. & Sternberg, A. 1996, *A&A*, 315, L281
 van der Tak, Floris F. S. 2006, *Royal Society of London Transactions Series A*, 364, 1848, 3101-3106
 van Dishoeck, E. F. 1988, *Rate Coefficients in Astrochemistry*. Editors, T.J. Millar, D.A. Williams; Publisher, Kluwer Academic Publishers, Dordrecht, Boston, 49.
 Wakelam, V. & Herbst, E. 2008, *ApJ*, 680, 371.
 Ward-Thompson, D., Nutter, D., Bontemps, S., Whitworth, A. & Attwood, R. 2006, *MNRAS*, 369, 1201.
 Williams, J.P., Bergin, E.A., Caselli, P., Myers, P.C. & Plume, R. 1998, *ApJ*, 503, 689.
 Wolfire, M. G., Hollenbach, D., McKee, C. F., Tielens, A. G. G. M. & Bakes, E. L. O. 1995, *ApJ*, 443, 152
 Wolfire, M.G., Tielens, A.G.G.M., Hollenbach, D. & Kaufman, M.J. 2008, *ApJ*, 680, 384.
 Woodall, J., Agúndez, M., Markwick-Kemper, A. J. & Millar, T. J. 2006, *A&A*, 466, 1197.
 Woods, R. C., Gudeman, C. S., Dickman, R. L. et al. 1983, *ApJ*, 270, 583.
 Wootten, A., Loren, R. B. & Snell, R. L. 1982, *ApJ*, 255, 160.
 Zhou, S., Jaffe, D. T., Howe, J. E., Geis, N., Herrmann, F., Madden, S. C. Poglitsch, A. & Stacey, G. J. 1993, *ApJ*, 419, 190.
 Ziurys, L. M. & Apponi, A. J. 1995, *ApJ*, 455, 73.